International Journal of Solids and Structures 50 (2013) 3430–3445

Contents lists available at SciVerse ScienceDirect

International Journal of Solids and Structures

journal homepage: www.elsevier.com/locate/ijsolstr

Impact against X65 steel pipes – An experimental investigation

Martin Kristoffersen [a,*], Tore Børvik [a], Ida Westermann [a,b], Magnus Langseth [a], Odd Sture Hopperstad [a]

[a] Structural Impact Laboratory (SIMLab), Centre for Research-based Innovation (CRI), Department of Structural Engineering, Norwegian University of Science and Technology, Rich. Birkelands vei 1A, NO-7491 Trondheim, Norway
[b] SINTEF Materials and Chemistry, Alfred Getz' vei 2, NO-7034 Trondheim, Norway

ARTICLE INFO

Article history:
Received 8 February 2013
Available online 26 June 2013

Keywords:
Pipe impact
Material tests
Impact tests
Fractography

ABSTRACT

Offshore pipelines subjected to accidental loads, such as impacts from trawl gear or anchors, may experience large global displacements from its initial position and large local strains. The axial forces set up during deformation move the pipeline back towards its initial position, thereby creating a complex local stress and strain history that may lead to fracture in the pipeline. In this study, material and component tests have been carried out on an X65 offshore pipeline material to investigate the behaviour during impact, and to observe if fracture occurs. Pipes were first impacted in a pendulum accelerator at varying velocities before they were pulled straight in a tension machine. Fracture was found in the impacted area of all the pipes. Material tests were carried out to determine the characteristics of the X65 pipeline material. A metallurgical investigation was also conducted, revealing that fracture initiated both inside the pipe wall and on the surface.

1. Introduction

Transportation of oil and gas is an essential part of the offshore industry. To this end, pipelines are under widespread use, often under high pressures and temperatures (Jones, 2010; Manes et al., 2012). Impacts from trawl gear and anchors are known to cause problems, see e.g. Statoil ASA (Cited 23.01.2013) where an anchor impacted a pipeline and dragged it far from its initial position after hooking it. The anchor chain eventually broke and the pipeline was subsequently released and straightened due to the large axial forces present. This necessitates an assessment regarding the hazards and potential damage following such an event (Jones and Birch, 1996) as failure in a pipeline transporting oil and/or gas could result in severe environmental damage and economic losses. A local dent caused by such an event may lead to a propagating buckle (Kyriakides and Netto, 2000), while the large global deformation sets up large forces as mentioned. The Petroleum Safety Authority of Norway has published a comprehensive list online of accidental damage on structures in the North Sea and Norwegian Sea (Ptil, Cited 23.01.2013).

Det Norske Veritas (DNV) has given guidelines on certification and verification of pipelines (DNV, 2000), a standard on general design of pipeline systems (DNV, 2008) and specified some recommended practice on interference between pipelines and trawl gear (DNV, 2010). The latter of these provides a critical load of a trawl clump weight of 9000 kg impacting the pipeline at 2.8 m/s. It also includes pull-over as well as possible hooking analysis. A load cycle of impact, pull-over and release produces a complex stress and strain history which is not well covered in the guidelines. In addition to the simplified analysis, the guidelines allow for use of numerical analyses and model tests in the design phase.

The open literature provides several studies on pipeline impact. Johnson, Reid and coworkers published a series of three papers on large transverse deformations of thin walled circular tubes (Thomas et al., 1976; Watson et al., 1976a,b). Thomas et al. (1976) did impact tests where a wedge was dropped onto the pipe's midspan. The energy required to reproduce the same magnitude of deflection quasi-statically was compared to the initial potential energy of the dropped object. Less energy was needed when deforming the mild steel pipes quasi-statically, typically 50% to 70% of the initial potential energy in the wedge. Energy transfer ratio increased with increasing dropping height, occasionally up to 90%. Fully clamped pipes have been studied by Jones et al. (1992) and by Chen and Shen (1998). Pressurized pipes were studied by Shen and Shu (2002); Ng and Shen (2006) and more recently by Jones and Birch (2010). Palmer et al. (2006b) considered concrete coated pipelines dropped on one another. Manes et al. (2012) attempted to recreate the loading sequence of impact, pull-over and subsequent release by subjecting plate strips of an actual offshore pipeline to quasi-static three point bending tests. The strips were then pulled straight and checked for fracture.

This study presents impact experiments on a simply supported pipe made from X65 steel, a material typically used for offshore pipelines transporting oil and/or gas (Oh et al., 2007). To gain a bet-

* Corresponding author. Tel.: +47 73 55 10 48; fax: +47 73 59 47 01.
E-mail address: martin.kristoffersen@ntnu.no (M. Kristoffersen).

0020-7683/$ - see front matter © 2013 Elsevier Ltd. All rights reserved.
http://dx.doi.org/10.1016/j.ijsolstr.2013.06.013

ter understanding of the material's behaviour, a material test programme was performed on specimens taken in different directions and from different locations across the pipe's cross-section. A pendulum accelerator, described in detail by Hanssen et al. (2003), was used to launch a trolley with a given mass and velocity against the pipe. No surrounding water was present, and no internal pressure was applied to the pipe. After the impact event the pipe was pulled straight in a tension rig. This is thought to represent the loading sequence of impact and straightening of a full-scale pipeline, albeit simplified in order to accommodate the experiments in the laboratory equipment available. The main physics of the problem should nevertheless be captured. In addition to providing experimental data on a pipe being struck and stretched, investigation on whether such a loading sequence would form cracks and/or fracture in the pipe wall was of particular interest. A metallurgical investigation including scanning electron microscopy (SEM) was therefore conducted on both deformed and undeformed material. Cracks discovered in the component tests were examined closely, and additional material tests were performed in an attempt to explain the fracture surfaces observed.

2. Material tests

2.1. Material description

The material in the pipes used in this study is similar to the X65 grade steel used by Manes et al. (2012), but the pipes are manufactured in a different manner. Where the pipes used by Manes et al. (2012) were formed from rolled plates and welded longitudinally, the current pipes are made seamless. A rough outline of the forming process is as following: By subjecting a solid metal cylinder to radial compression, a cavity forms along the cylinder's longitudinal axis. This is known as the *Mannesmann effect* (Ghiotti et al., 2009). The cylinder is then pierced, thus expanding the cavity to form a shell. This shell is then worked to the desired specifications in terms of diameter and thickness. The production of the pipeline has been in accordance with the guidelines in DNV-OS-F101 (DNV, 2008) by the Argentinean supplier Tenaris. Further details can be found in Tenaris' documentation (Tenaris, Cited 23.01.2013). Variations in the production method may give rise to different material properties, hence a new material test programme was conducted as described below.

All specimens used in the material tests (and the component tests presented in Section 3) in this study were taken from the same continuous pipe, which had an initial length of approximately 12 m. According to the material inspection certificate, the nominal yield stress and the ultimate tensile strength are 450 MPa and 535 MPa, respectively. Young's modulus is 208000 MPa. The inner diameter of the pipe is 123 mm, and the nominal wall thickness 9.5 mm, making the outer diameter 142 mm and the diameter to thickness ratio approximately 13. Aside from Fe, the main chemical constituents of this alloy are 0.09 C, 0.25 Si, 1.13 Mn, 0.04 Cr, 0.09 Mo, 0.09 Cu and 0.06 V (numbers in weight percentage).

From an energy-dispersive X-ray spectroscopy (EDS) of the matrix, it was evident that it contained Fe, Mn and C, as expected from the material inspection certificate. SEM investigations of the undeformed material revealed two types of particles; spherical and angular (both seen in Fig. 1). A diameter of about 2 μm to 25 μm was found for the spherical particles, and they were inhomogeneously distributed in the matrix. They consisted mainly of calcium aluminate, and bonded poorly with the matrix. The angular particles, while much less numerous, bonded well with the matrix and their typical size was about 5 μm. Titanium was the main component of these particles, with carbon or nitrogen (inconclusive) second. The microstructure of the undeformed material seen in Fig. 2 was similar in both the radial and longitudinal direction of the pipe, and it has a ferritic grain structure with grains of size $\leqslant 10$ μm.

2.2. Experimental programme

The pipe material's cross-section homogeneity and possible anisotropic yielding properties were the characteristics sought by the material test programme in this study. To examine the section homogeneity, tensile specimens were cut from different locations – dubbed north, south, east and west – across the cross-section of the pipe. Being seamless, the pipe has no natural reference point on the cross-section, so one was chosen at random. As the material may have anisotropic properties, specimens were cut in three different directions with respect to the pipe's longitudinal axis; 0°, 45° and 90°. Fig. 3(a) makes evident the positions and directions from where the specimens were cut. These specimens were tested quasi-statically in tension.

2.3. Uniaxial tensile tests

Tensile tests were carried out at quasi-static strain rate and room temperature on smooth axisymmetric specimens, whose geometry can be seen in Fig. 3(b). The chosen geometry should, based on the images in Fig. 2 from the light optical microscope, be large enough to sample a representative portion of the material. A displacement controlled Zwick testing machine was used with a constant deformation rate of 0.3 mm/min. This corresponds to an initial strain rate of $\dot{\varepsilon} = 10^{-3}\ \mathrm{s}^{-1}$ using a gauge length of 5 mm. Two tests from each of the positions across the cross-sections (north, south, etc.) and two from each of the directions (0°, 45° and 90°) were performed.

During testing, the force, the cross-head displacement and the specimen's diameter reduction were continuously measured. A laser based measuring device was used to measure the diameter reduction until fracture (i.e. also after incipient necking). Two perpendicular lasers (AEROEL XLS13XY with 1 μm resolution) executed the measuring with great accuracy. The lasers were mounted on a mobile frame to ensure that the diameters were always measured at minimum cross-section. With diameter reduction measurements it is possible to calculate the true stress σ and the true logarithmic strain ε through the formulas

$$\sigma = \frac{F}{A} \tag{1}$$

$$\varepsilon = \ln\left(\frac{A_0}{A}\right) \tag{2}$$

where F is the force measured by the load cell on the Zwick machine and A_0 is the specimen's initial cross-sectional area calculated by $A_0 = (\pi/4)D_0^2$, D_0 being the initial diameter. A is the current area of the cross-section, obtained by

$$A = \frac{\pi}{4} D_1 D_2 \tag{3}$$

in which D_1 and D_2 are the diameters measured by the two lasers. Assuming additive decomposition of the elastic and plastic strains, the plastic strain can be found through the relation $\varepsilon^p = \varepsilon - \sigma/E$ where E is Young's modulus. It should be noted that plastic incompressibility and negligible elastic strains are assumed in Eq. (2), and that after necking the stress σ and strain ε represent average values over the minimum cross-section.

Results from the section homogeneity tests (one from each of the positions) are presented in Fig. 4(a), plotted as true stress vs. true strain. These curves are similar to those for the X65 steel used by Hyde et al. (2007) in their study of longitudinal indentation of unpressurised pipes. The scatter between each individual test from

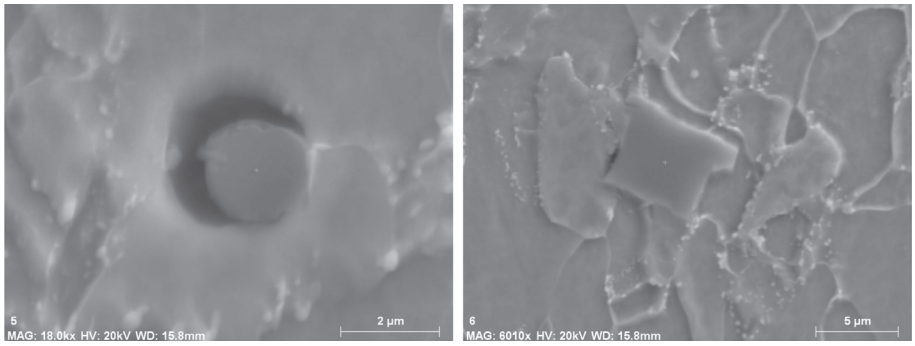

(a) Spherical particles (b) Angular particles

Fig. 1. Pictures from the electron probe microanalysis of the two types of particles found in the material.

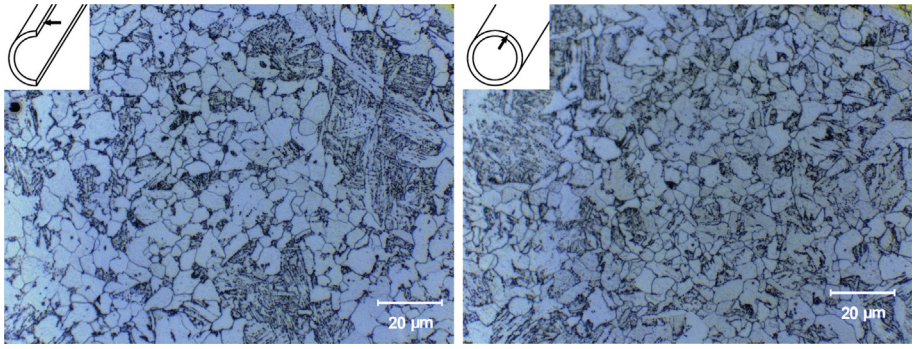

(a) Radial direction (b) Longitudinal direction

Fig. 2. The microstructure of the material in undeformed condition taken from the pipeline, at $\times$ 100 magnification.

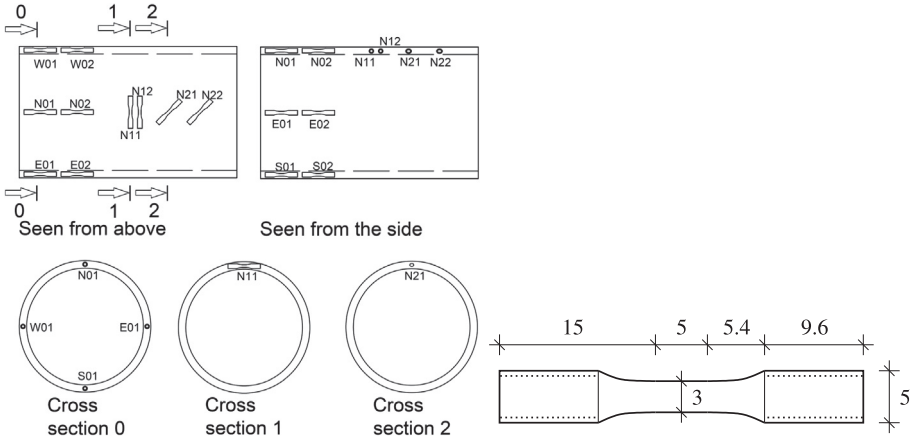

(a) Specimen locations (b) Specimen geometry

Fig. 3. Figure (a) shows the locations and directions from which test specimens shown in (b) were cut.

each position was low, and the same applies to the directional tests. Based on average values from 12 tests, the material yields at 478 ± 15 MPa and has a nominal peak stress of 572 ± 14 MPa, strain hardens to a true peak stress of 1314 ± 12 MPa and fails at a true strain of 1.61 ± 0.03 by a ductile cup-and-cone fracture. The data from the tests, along with the fracture surfaces shown in Fig. 5(a)–(d), strongly suggest that for practical and design applications the material properties are homogeneous across the cross-section.

True stress-true strain relations from the tests at different directions (one from each direction) are displayed in Fig. 4(b), showing the same tendencies; yielding at almost 500 MPa and a peak true stress of about 1300 MPa. The fracture strain was also of the same magnitude, approximately 1.6. Again the data is quite conclusive; no anisotropy appears to be present, as the circular fracture surfaces in Fig. 5(e)–(f) also indicate. Based on these results, the material will henceforth be treated as isotropic and homogeneous, in contrast to the quite anisotropic appearance of the X65 steel used by Manes et al. (2012).

3. Component tests

3.1. Setup

The experimental setup is an attempt to recreate the loading scenario where a pipeline is first hit and displaced by an impacting

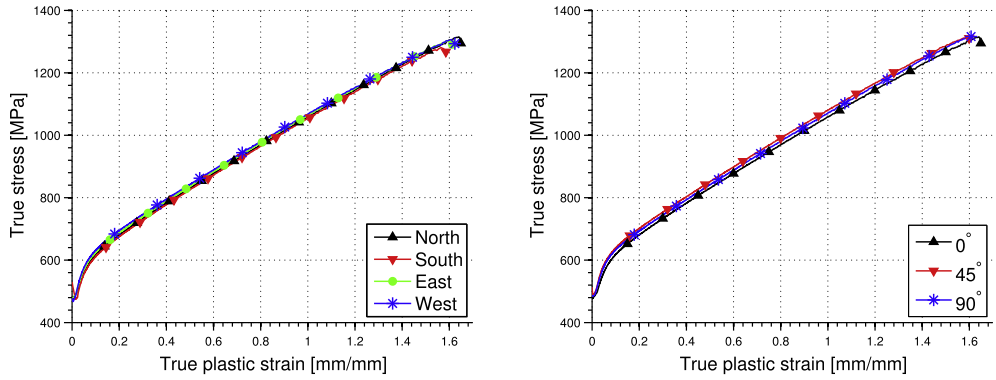

(a) Section homogeneity (b) Anisotropy

Fig. 4. Data from quasi-static tensile tests on uniaxial specimens.

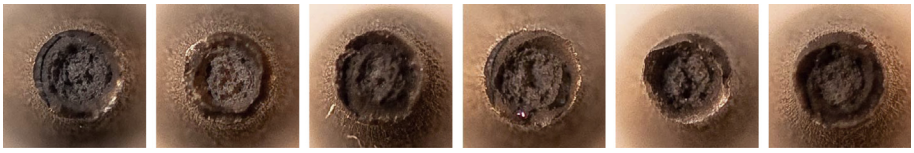

(a) North 0° (b) West 0° (c) South 0° (d) East 0° (e) North 45° (f) North 90°

Fig. 5. Fracture surfaces from different tensile test specimens.

object before being released and straightened as a consequence of rebounding caused by the presence of global axial forces. The experiments consist of two main steps. A simply supported pipe is first struck by a trolley with a given mass and velocity in a pendulum accelerator. The pendulum accelerator is described in detail by Hanssen et al. (2003). Next, the pipe is straightened quasi-statically in a standard 1200 kN Instron universal testing machine using bolts through the unlathed end sections of the pipe, leaving it free to rotate. The former part represents the impact, while the latter is thought to correspond to the rebound and straightening of the pipeline. These steps are a simplification of the actual load events, but will serve as indicators as to what may happen in a real case.

Fig. 6 illustrates the difference between the actual impact scenario and the experiment, with the actual event divided in three stages. The first part is when the impactor hits and creates a local dent. Large global deformations are then caused by a continuation of the impact and hooking of the pipeline. These two steps occur

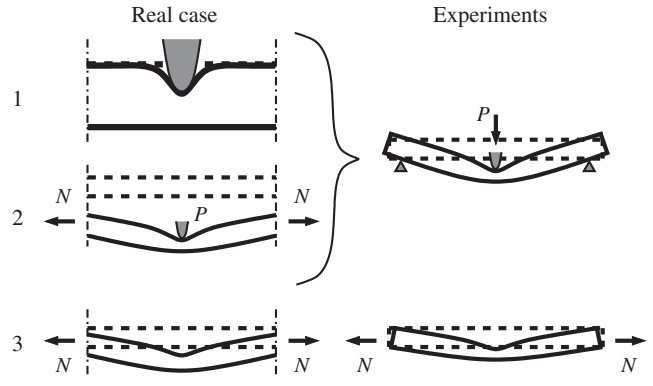

Fig. 6. Comparison of reality and experiments, respectively the left and right part of the figure. The dotted lines indicate the initial position, while the solid lines signify the displacements. Stage 1 is zoomed in for clarity, and the sketch is not to scale.

simultaneously in the laboratory experiments. As the pipeline is displaced in the real case, axial forces (labelled N in Fig. 6) arise as a consequence. These axial forces will in the current tests not be present due to the test pipe being simply supported, which is one simplification. When the pipeline is finally released in the real case, the axial forces move it towards its initial position. This corresponds to the stretch part of the experiments. Although the actual case and the tests differ somewhat, the experiments should capture the main physics of the problem. Eight pipes were tested in total, with no surrounding water and no internal pressure. The first six pipes, labelled A through F, were impacted at different velocities and subsequently stretched. Two pipes, called K and L, were exposed to the impact part of the test only. This was done to make bent pipes available for a metallurgical study.

As indicated, an actual piece of a pipeline (albeit of decreased length to make it fit the test rig) was used as test component. Vital test parameters, like the free span of the pipeline, the trolley's mass and impact velocity, indenter shape and the pipe's thickness, were designed by means of numerical simulations and the guidelines given by DNV (2010). A schematic sketch of the impact test setup is shown in Fig. 7. It has been noted, as one might expect, that a pointed indenter pierces the pipe more easily (Palmer et al., 2006a). For that reason the sharpest indenter given in the guidelines was chosen. The pipe was given a total length of 1300 mm, a free span of 1000 mm and a nominal thickness of 4 mm, resulting in a D/t ratio of about 30. This ratio is approximately the same as in many pipelines in use for oil and gas transportation (Manes et al., 2012) as well as in the tubes used by Thomas et al. (1976). To achieve this thickness the pipe was lathed down from 9.5 mm to 4 mm, thus introducing a slightly uneven surface and wall thickness over the cross-section. The thickness of the different pipes were measured by a portable ultrasound device and measurements were taken at multiple locations across each pipe.

The trolley was assigned a mass of 1472 kg and an initial velocity v_0 in the range of approximately 2.5 and 5.0 m/s, representing the trawl velocity (DNV, 2010). Pictures of the test setup are shown in Fig. 8, where (a) shows the impact part of the experiments and

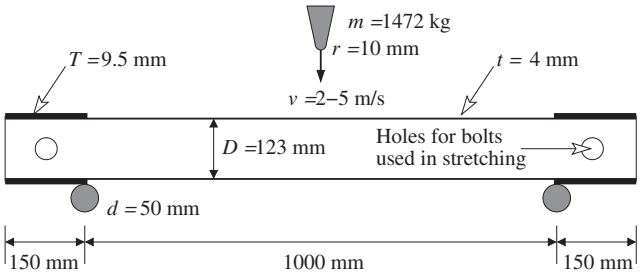

Fig. 7. Schematic sketch of impact part the component test, which corresponds to stage 1 and 2 from Fig. 6.

(b) the stretching phase after the impact. If the global deformation of the pipe was too small after the impact, the tension step afterwards would require a very high axial load in order to see some straightening effect. For that reason, it was important to produce a global deformation sufficiently large (of the order of the pipe's radius). The supports in the impact phase were massive cylinders with a diameter of 50 mm, while the hardened nose of the trolley (the part making contact with the pipe) had a radius of 10 mm. A load cell located between the nose and the trolley was used to sample the contact force during impact (Hanssen et al., 2005). In addition, aluminium crash boxes were set up as buffers to limit the maximum transverse deformation of the pipes.

3.2. Results

Force–displacement curves for all pipes A through F during both impact and subsequent stretching are plotted in Fig. 9. As seen, the scatter is very low. The curves for e.g. pipes A and B are virtually identical, meaning that initial velocity exerts little or no influence on the shape of the curve. As long as the mass ratio between the trolley and the pipe is large (i.e. the inertia of the pipe becomes negligible), it seems that the strain rates in this velocity range have no significant influence on the measured contact force between the impactor and the pipe. When testing pipes B and E the trolley hit the buffer in the rig, hence the matching maximum displacement. The peak force in the impact tests (see Fig. 9(a)) averaged at 73.1 ± 2.5 kN. The force increases in the beginning when the deformation is still local, and starts to decrease when a transition is made from local to global deformation, which suggests another explanation for the peak loads being similar despite the different initial velocities. The remainder of the kinetic energy after the peak is attained, is mainly absorbed by global deformation.

The deformation pattern observed corresponds well with the three modes of deformation identified by the quasi-static three-point bending tests on tubular components with similar D/t-ratio by Thomas et al. (1976). These modes are crumpling, crumpling and bending, and finally structural collapse. Increasing the velocity from 3.24 m/s (pipe A) to 4.14 m/s (pipe E) resulted in the largest jump in final transverse deformation (from 170 mm to 330 mm), indicating that a transition from crumpling and bending to structural collapse occurs in this velocity interval.

From Fig. 9(b) it is clear that higher initial velocity, and thereby higher deformation after impact, produces a much lower force level during stretching. The machine stiffness in the tension rig was measured by placing a massive, rigid cylinder in the machine and loading to slightly above the maximum force from the stretch tests. Any deformation measured is then in the machine, and this was subtracted from the original results. When the stretching phase initiates, the least deformed pipes can take the applied load as axial forces almost immediately, while the most deformed ones have to withstand a bending moment first due to their large global deformation. After being straightened, the oval shape of the pipes became quite circular, which can make impacted zones hard to detect, especially if no visible cracks or dents are present. As will be shown in Section 4.1, the most deformed pipes received a significant crack already after impact only. Photo series at 5000 frames per second obtained by a highspeed camera of type FASTCAM SA1.1 model 675 K-M1 can be seen in Fig. 10(a) and (b), which

(a) Impact testing (b) Stretch test of pipe B

Fig. 8. The component tests' (a) impact phase, and (b) stretch phase.

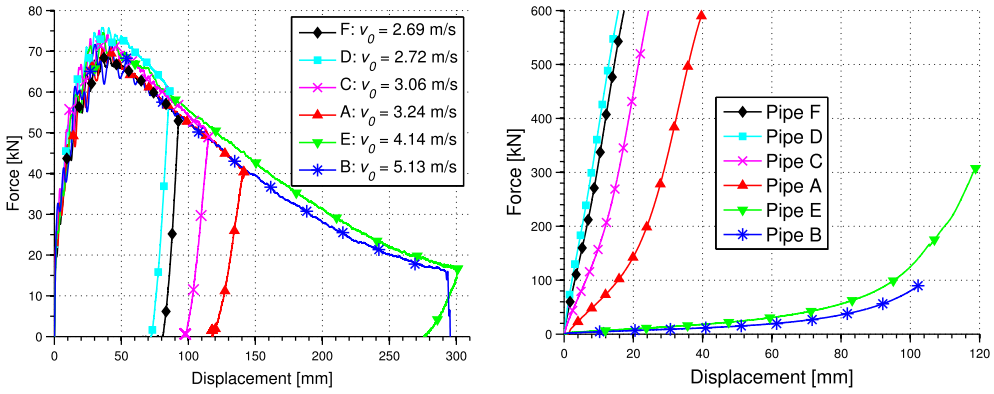

(a) Impact data (b) Stretch data

Fig. 9. Results from (a) the impact tests, and (b) the stretch tests sorted by impact velocity. It should be noted that the stretch data does not account for the increased moment arm caused by the deformation from the impact. Deformations in the tension machine has been subtracted in the stretch data based on the measured machine stiffness.

show pipes A and B respectively. The test setup showed very good repeatability, and some important parameters from the experiments are listed in Table 1 with an illustrative legend in Fig. 11. Data for pipes K and L used for metallurgical investigations were very similar to that of pipes B and A, respectively.

In the impact phase, the pipe was aligned so that it was struck on the side labelled north, and all pipes deformed well into the plastic range. Fracture was observed by visual inspection in all pipes during the stretch phase, but at very different load levels, ranging from a maximum value of 274 kN to just after stretching was initiated (about 10 kN judged by visual inspection during stretching) for the most deformed pipe. Due to the large differences in deformation, different cross-head velocities were used during stretching, but was always kept in the quasi-static regime. During stretching, pipe B ($v_0 = 5.13$ m/s) ruptured through the entire thickness of the pipe wall (shown in Fig. 12(a) and (b)). A visual inspection of pipe A ($v_0 = 3.24$ m/s) revealed only surface cracks and not through-thickness failure (Fig. 12(c)). The through-thickness crack has three distinct zones as indicated by the numbers on the picture in Fig. 12(b):

Zone 1: The impact side of the pipe.
Zone 2: The side opposite to the impact side.
Zone 3: The transition zone between the two first zones.

Looking at Fig. 12(c), traces of the pipe being milled down are visible and fracture appears to initiate at the bottom of these traces. An uneven surface may lead to stress and strain concentrations, thereby initiating cracks at specific locations, but as will be shown this is believed to be of minor importance for the fracture process itself.

4. Fracture investigations

The undeformed material is described in Section 2.1, whereas this section will focus on the deformed and fractured material subjected to different loading conditions, taken from the component tests as well as additional material tests on notched specimens. The samples were examined using an optical light microscope and a scanning electron microscope.

The metallurgical investigations are divided in three parts. The first part is comprised of the samples taken from the pipes used in the component testing. The material was examined after two different load cases: impact and stretching, and impact only. The sec-

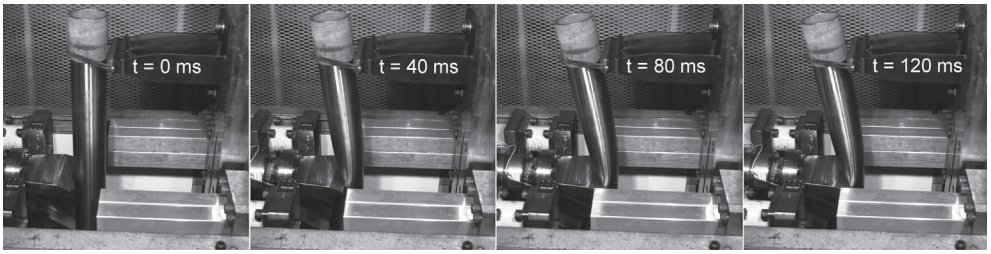

(a) Pipe A, $v_0 = 3.24$ m/s

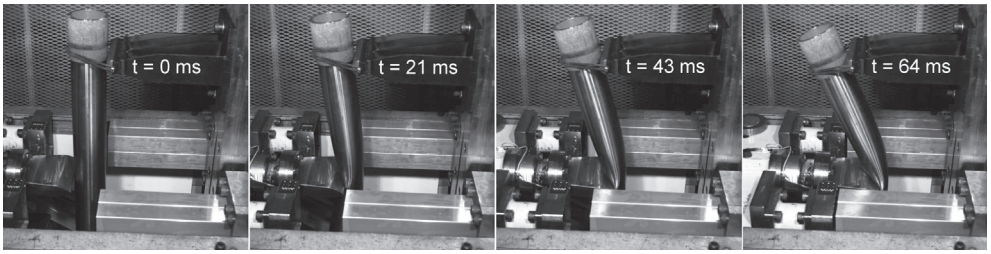

(b) Pipe B, $v_0 = 5.13$ m/s

Fig. 10. The impact phase of the component tests, examplified by (a) pipe A and (b) pipe B.

Table 1
Experimental matrix for component tests. See Fig. 11 for explanation of measurements.

Pipe		A	B	C	D	E	F
Trolley mass	[kg]	1472	1472	1472	1472	1472	1472
Nose radius	[mm]	10	10	10	10	10	10
Avg. thickness	[mm]	3.89 ±0.36	3.86 ±0.34	4.04 ±0.18	4.26 ±0.38	4.19 ±0.32	4.09 ±0.30
Impact test results							
Initial velocity	[m/s]	3.24	5.13	3.06	2.72	4.14	2.69
Kin. energy	[J]	7708	19356	6875	5435	12613	5316
Abs. energy	[J]	7294	11736	6520	5096	12503	5083
Peak force	[kN]	70.7	72.7	75.1	75.8	74.6	69.7
w_i	[mm]	170	333	142	105	330	101
L_{N-N}	[mm]	1250	1104	1267	1286	1123	1288
d_{N-S}	[mm]	60	22	71	86	25	98
d_{E-W}	[mm]	180	199	172	162	195	159
α	[deg]	12	30	9	3	30	3
Stretch test results							
Def. rate	$[\frac{mm}{min}]$	20	20	5	5	10	5
Max. force	[kN]	590	90	602	601	307	601
Fracture force*	[kN]	100	10	146	274	24	269

*Determined by visual inspection during stretching.

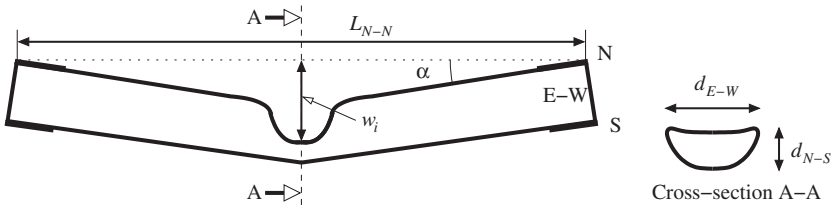

Fig. 11. Typical outline of deformation shapes of pipes after impact load at midspan (not to scale), along with explanation of measurements given in Table 1.

ond subsection concerns notched compression-tension samples. Finally, notched specimens subjected to compression only have been investigated. The additional material tests will be presented along with the results from the microscopy.

4.1. Samples from component tests

4.1.1. Impact and stretching

Firstly, the fracture surfaces from the pipes impacted and straightened were investigated to see what kind of fracture mechanisms that were present after the entire loading sequence described in Section 3. Visible fracture surfaces from the pipes were inspected, so the samples were taken from the pipes' most deformed area. Two main types of macroscopic cracks were present after impact and stretching; through-thickness cracks (Fig. 12(b)) and and cracks on the pipe's surface (Fig. 12(c)). The through-thickness cracks had three different zones as mentioned above.

Fig. 13(a) shows the fracture surface of zone 1, exhibiting a classic cleavage fracture (Anderson, 2005). These cracks were the first to appear during stretching, almost immediately after applying the load. Zone 2, seen in Fig. 13(b), has a fracture surface of a completely different character – a mixture of small and large dimples along with spherical particles (typically located at the bottom of the dimples) are observed, thus indicating a ductile fracture. This part of the crack propagated at a later stage during the stretch part of the experiments. The final zone is a ductile "ridge" (framed by a black rectangle in Fig. 14(a)) in the transition from the ductile to the cleavage fracture surface. Large dimples with particles were observed along this edge, seen in Fig. 14(b). Cracked particles were also present, examplified by Fig. 14(c). A close up of one of the dimples with particles is offered in Fig. 14(d). It appears that voids initiate around the spherical particles (sometimes cracked), which bonded poorly with the matrix.

In addition to the through-thickness cracks, there were also surface cracks. These were also inspected in the SEM, and a ductile fracture with directional voids, typical of tearing, was found. The surfaces were very similar in nature to that of zone 2, seen in Fig. 13(b).

4.1.2. Impact only

Two additional pipes were subjected to impact, one in the upper end of the velocity spectrum (pipe K, 5.18 m/s) and one in the middle (pipe L, 3.26 m/s), corresponding to pipe B and A, respectively. These were not exposed to stretching, thus allowing investigation of potential damage after impact only. Samples were once again cut from the dent where the trolley hit the pipes. Macroscopic inspections of pipe K revealed a clearly visible crack in the dent where the nose of the trolley hit. The crack ran through 75% of the pipe wall's thickness (pictured in Fig. 15(a)). This crack probably emerged during the springback after the impact. Investigation of the microstructure in the optical microscope disclosed a mixed fracture type (intercrystalline and transcrystalline) after large deformations (Fig. 15(c)). Further investigation showed that the grains were much less deformed at the end of the crack tip. This indicates that the outer side of the pipe wall facing the impactor suffers more deformation than the inner side.

A cross-section of the pipe at the outer edge of the dent created by the trolley's nose, where the crack no longer was visible on the surface, was also investigated. Internal cracks were found through 75% of the wall thickness, as seen in Fig. 15(b). These cracks did not connect with any surface cracks either, and may therefore be difficult to detect when inspecting a pipeline after an impact event.

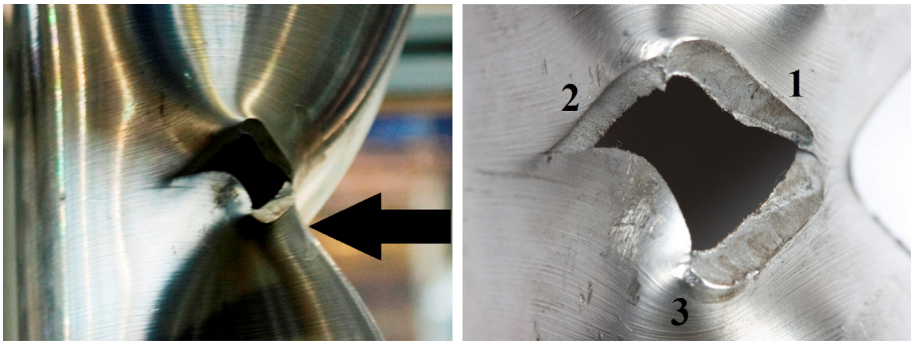

(a) Overview of pipe B (b) Through-thickness crack in pipe B

(c) Surface cracks in pipe A

Fig. 12. Photographs of (a) impact zone in pipe B with an arrow signifying the impact direction and location, (b) close-up of through-thickness crack in pipe B and (c) surface crack in pipe A. All images are taken after impact and stretching.

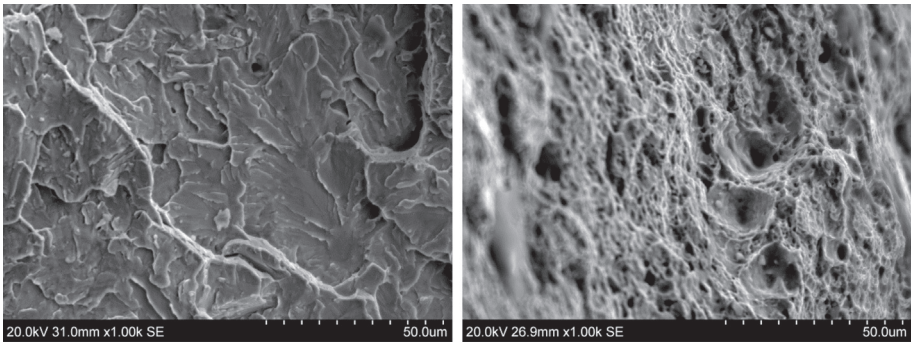

(a) Zone 1 × 1000 (b) Zone 2 × 1000

Fig. 13. SEM images of (a) cleavage fracture in zone 1, and (b) ductile fracture in zone 2, both taken from pipe B.

This is also why the traces from the milling process are thought to be of minor importance. An intercrystalline fracture was found, with no large deformation of the material's microstructure, shown in Fig. 14(d). The fracture surfaces from this test (indicated by the white arrow in Fig. 15(a)) were also investigated in the SEM, revealing a brittle cleavage fracture of the same character as seen in Fig. 13(a).

The pipe impacted at 3.26 m/s showed no immediate tendency to crack initiation, neither by visual inspection nor in the optical microscope. The surface was intact and no internal cracks were seen. Four samples were cut from the impacted area, all of which are shown in Fig. 16. Sample 1 showed no signs of fracture at any magnification. Investigation of the second sample, shown in Fig. 17(a), revealed a latent crack approximately 300 μm long in the middle of the material thickness, where the traces from the milling exerts little or no influence. The crack was found around the grain and phase boundaries, and can be very hard to detect. Deformation of the microstructure appears to be small (compare Fig. 17(a) to Fig. 2). Surface cracks of about 50 μm were observed at the impact side in sample 3, as shown in Fig. 17(b). These may be initiated by the traces arising from the milling process. Hard phases can be seen near the surface in connection with the cracks,

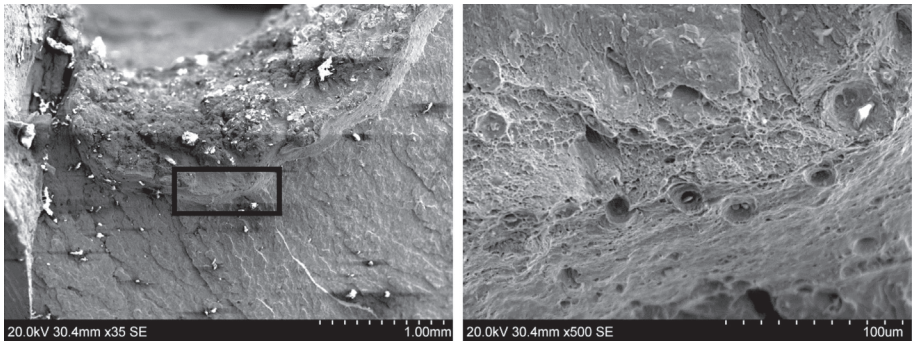

(a) Ductile "ridge", × 35 (b) Large dimples, × 500

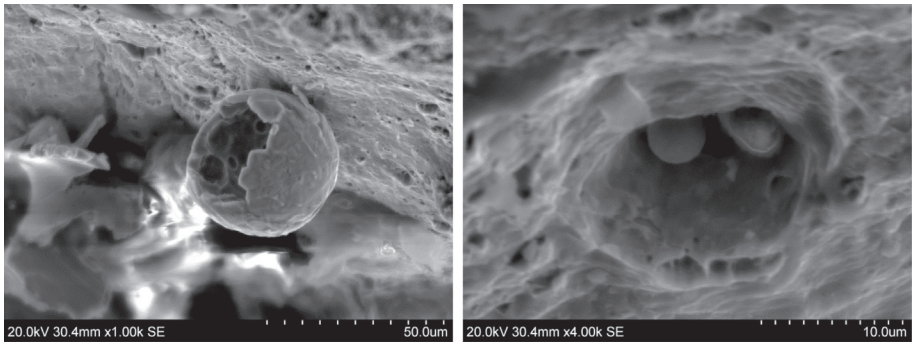

(c) Cracked particle, × 1000 (d) Dimple with particles, × 4000

Fig. 14. SEM images of the transition zone (zone 3) between brittle and ductile fracture surfaces.

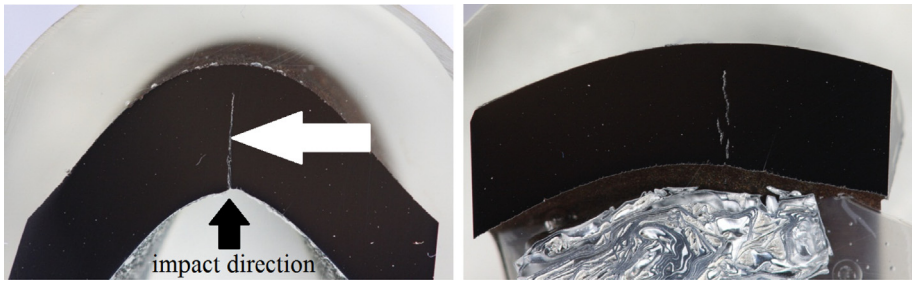

(a) External crack (b) Internal crack

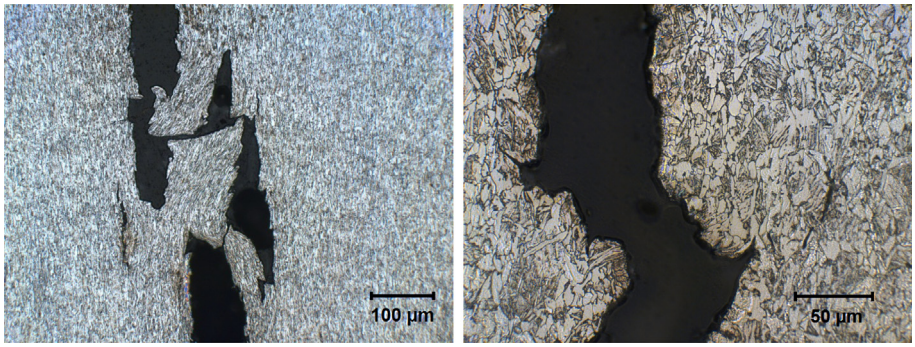

(c) Fracture at × 20 (d) Microstructure and crack at × 50

Fig. 15. External crack ((a) and (c)) and internal crack ((b) and (d)) found in pipe K subjected to impact at 5.18 m/s. SEM investigation of the fracture surface indicated by the horizontal arrow in (a) suggested a cleavage fracture.

but as this investigation is conducted on a 2D plane, it is difficult to say with certainty whether or not such phases are significant with respect to crack initiation. In sample 4 internal cracks were found along grain boundaries, with lengths of approximately 20 μm. All the cracks were located towards the impact side of the pipe wall.

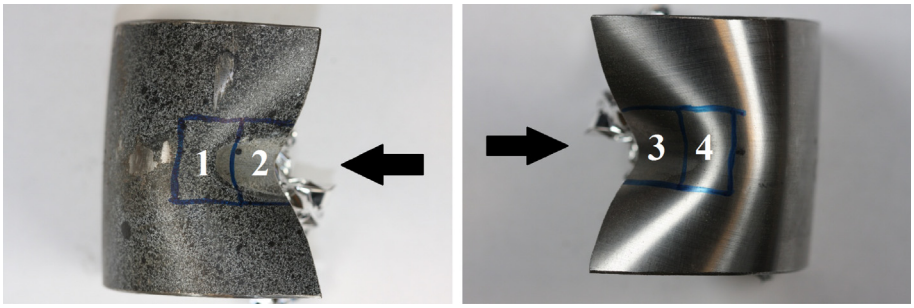

(a) Overview of samples 1 and 2 (b) Overview of samples 3 and 4

Fig. 16. Overview of samples taken from pipe L subjected to impact at 3.26 m/s. The arrows point to the side inspected in the microscope.

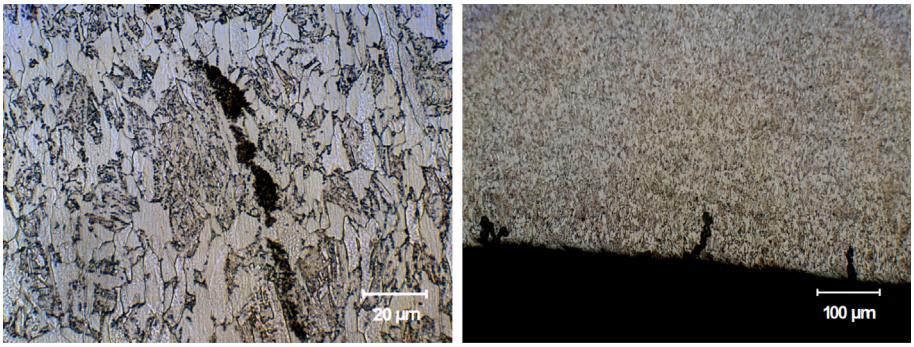

(a) Crack from sample 2, × 100 (b) Surface cracks in sample 3, × 20

Fig. 17. Internal crack (a) and surface cracks (b) found in samples taken from pipe L subjected to impact at 3.26 m/s.

4.2. Notched compression-tension tests

During impact the pipeline appears to suffer large compressive strains in the dent where the impactor hits, before being exposed to tension in the course of the springback and the following stretching. To shed some light on the material's behaviour under such loading conditions, experiments on notched specimens (shown in Fig. 18(a)) were performed in a deformation controlled Instron 100 kN testing machine. A similar study was conducted by Bao and Treitler (2004) on an aluminum alloy, which displayed a decrease in ductility with increasing compression. A contrary conclusion was reached by Bouchard et al. (2008) after exposing two different ductile steel grades to compression-tension loading. Based on the component tests, the ductility is expected to decrease with increasing compression before tension as a transition from ductile to brittle fracture is observed in this zone.

Based on numerical simulations, the geometry shown in Fig. 18(a) was chosen in an attempt to avoid possible buckling during the compressive phase. First, the specimens were compressed to different levels of large plastic strain – two of each specimen to 10%, 20%, 30% and 40% – before being stretched in tension to failure. The specimens' change of diameter was measured by the same technique as for the tension tests. Two additional specimens were stretched to failure without compression for reference, making two series of five specimens each.

True stress-true strain curves are presented in Fig. 18(b). The scatter between the two parallel test series from 0% to 40% compression was negligible. In tension only, the true stress-true plastic strain curve has a clear concave shape. This is not true for the specimens compressed first, which exhibit a slight decrease in work hardening rate before approaching their respective asymptotes. The transient Bauschinger effect is observed through the early onset of re-yielding for the reversed load. Towards the end of the tensile phase, all the curves tend to become almost parallel including the specimens loaded in tension only. Circular and ductile cup-and-cone fracture surfaces were observed for all specimens. The area A_f of the fracture surfaces increased with increasing compression, causing the "absolute" fracture strain $\varepsilon_f = \ln(A_0/A_f)$ to decrease as seen in Fig. 19(a). The "relative" fracture strain ε_r, obtained by using the area at load reversal A_r as reference rather than the initial area, also exhibits a drop with increasing compression. From Fig. 19(b) it is however seen that the effect on the relative fracture strain is smaller.

The fracture surfaces of the notched compression-tension specimens were examined using scanning electron and optical light microscopes. Using the SEM, a mixture of large and small dimples was found in the centre. Further, shear lips were present in the region near the outer surface in accordance with the cup-and-cone fracture. At 250 times magnification, the larger dimples appear to be deeper in the uncompressed specimen than those in the ones loaded in compression first (see Fig. 20), indicating that voids can grow to larger extents with less compression – a signal that ductility is being reduced (Ghajar et al., 2013). In specimens compressed to 20%, 30% and 40% the calcium aluminate particles are clearly seen in the large dimples, suggesting once again that voids initiate around these particles in compression (Sabih and Nemes, 2009). After compression, the stress level is considerably higher and the hardening similarly lower. This could lead to earlier void nucleation and accelerated void growth and coalescence by interligament necking at an early stage.

In Fig. 21(a) the magnification is increased to 1000 times, revealing calcium aluminate particles in all the large dimples. No

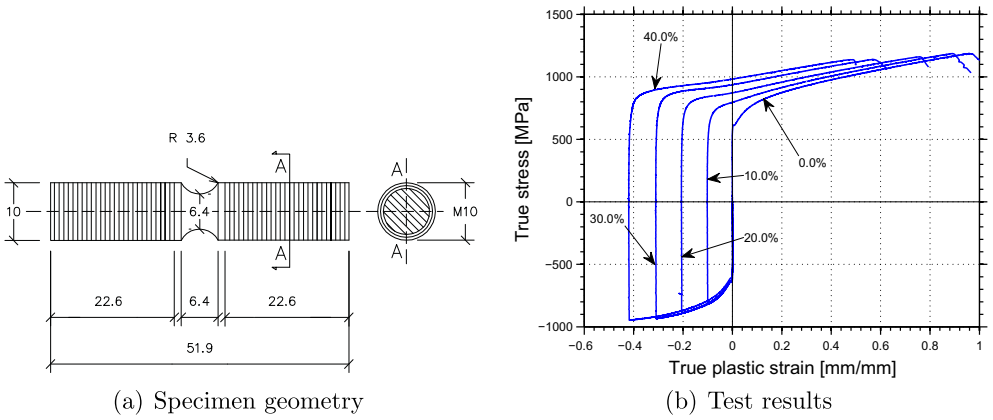

(a) Specimen geometry (b) Test results

Fig. 18. Specimen geometry (a) and results (b) from the first test series of notched compression-tension tests.

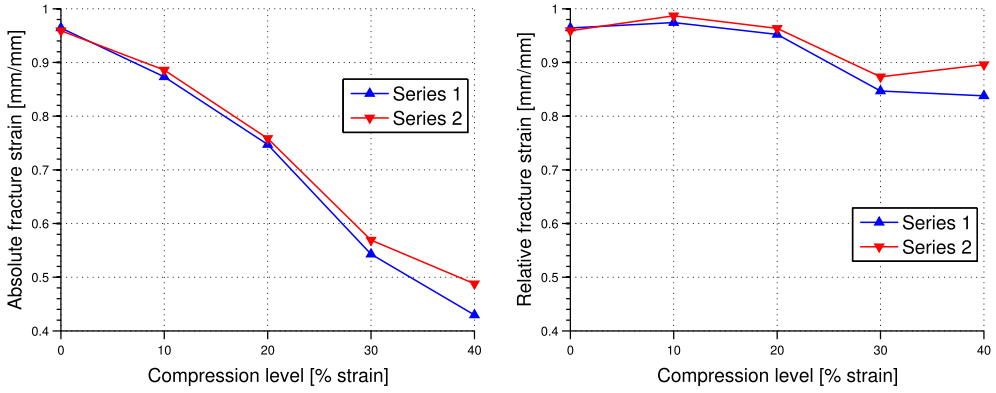

(a) Absolute fracture strain (b) Relative fracture strain

Fig. 19. Absolute (a) and relative (b) fracture strain vs. compression level from compression-tension tests on specimen shapes from Fig. 18(a).

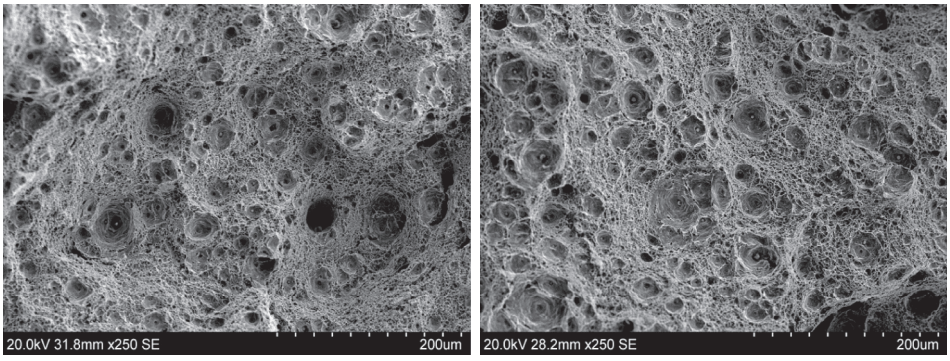

(a) 0% compression, deep dimples (b) 40% compression, shallow dimples

Fig. 20. SEM images of fracture surfaces of notched compression-tension specimens at × 250 magnification.

specific difference was found between the different magnitudes of compression at this magnification level. Compression before tension is expected to damage or fracture the spherical particles, and such a phenomenon was observed here. This has been reported in the literature e.g. by Cottrell (1959). By increasing the magnification to 3500 times, cracked particles are clearly visible, displayed in Fig. 21(b).

A further inquiry was made using a light optical microscope; the sample compressed to 40% was investigated along with the reference 0% specimen. Both specimens were cut through the center along the longitudinal axis, making the fracture surface's profile and the specimen's inner surface available for inspection. Before they were placed in the microscope, they were ground and polished to 1 μm. Fig. 22(a) and (b) show that voids have formed in a zone near the fracture surface in both the 0% and 40% specimens. These voids become visible during tension but may initiate during compression, as will be explained in Section 4.3. Fig. 22(c), showing the 0% sample at 50 times magnification, displays a somewhat blurry edge compared to what is seen in Fig. 22(d), which shows the corresponding 40% sample at the same magnification. This suggests a less ductile fracture in the 40% specimen. Also, the voids in this specimen are more spherical compared to the more rhombus

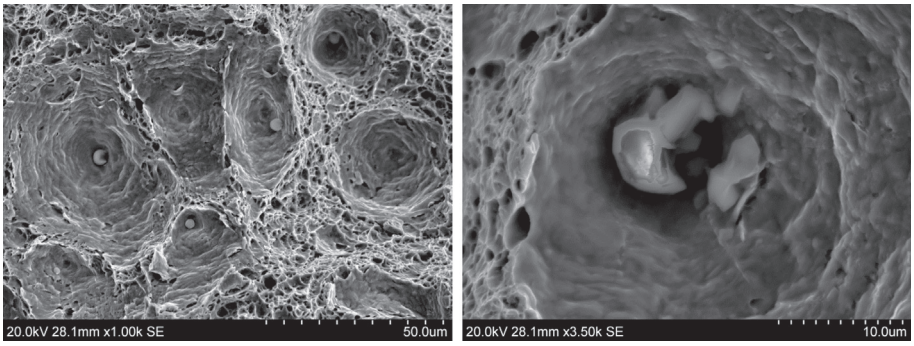

(a) × 1000 (b) × 3500

Fig. 21. SEM images of cracked particles in the specimen compressed to 40% at different magnification levels.

shaped voids of the 0% test. This indicates a more even pore growth when tension is preceded by compression. Voids may initiate around particles and expand perpendicularly to the load direction during compression, and along the load direction during tension. From Fig. 22(c) so-called ductile "fingers" are indentified in the 0% test. The 40% instance, on the other hand, has no such indications of ductility, made clear by the straight edges on the fracture surface in Fig. 22(d).

The microstructure also revealed another distinct difference between 0% and 40% compression when etched in nital. The grains are deformed and elongated to a much larger extent without the initial compression. Relative deformation is therefore decreased in the samples exposed to compression first. Both samples' microstructures at failure are shown in Fig. 23, while the undeformed microstructure can be seen in Fig. 2. Defects like voids and particles of size 5–40 μm were observed in the specimen exposed to tension only, while the one compressed to 40% before tension showed such defects ranging from 5 to about 90 μm. Both cases are shown in Fig. 23, but be aware that this is a 2D representation of a 3D material, so the darker areas seen might as well be distorted areas in the vicinity of the calcium aluminate particles.

Compression to 60% was attempted, but barreling of the specimen prohibited valid test results from being obtained – the specimen failed in the threads during tension due to the cross-section being widest in the area where the notch had initially been. Therefore a change was made in the specimen geometry; the cross-sectional diameter was reduced (shown in Fig. 24(a)) to postpone the onset of this barreling, which was incipient in the 40% specimens of the primary geometry. Two of each of the new specimens were compressed to true strain values of 40%, 60%, 80% and 90%, with

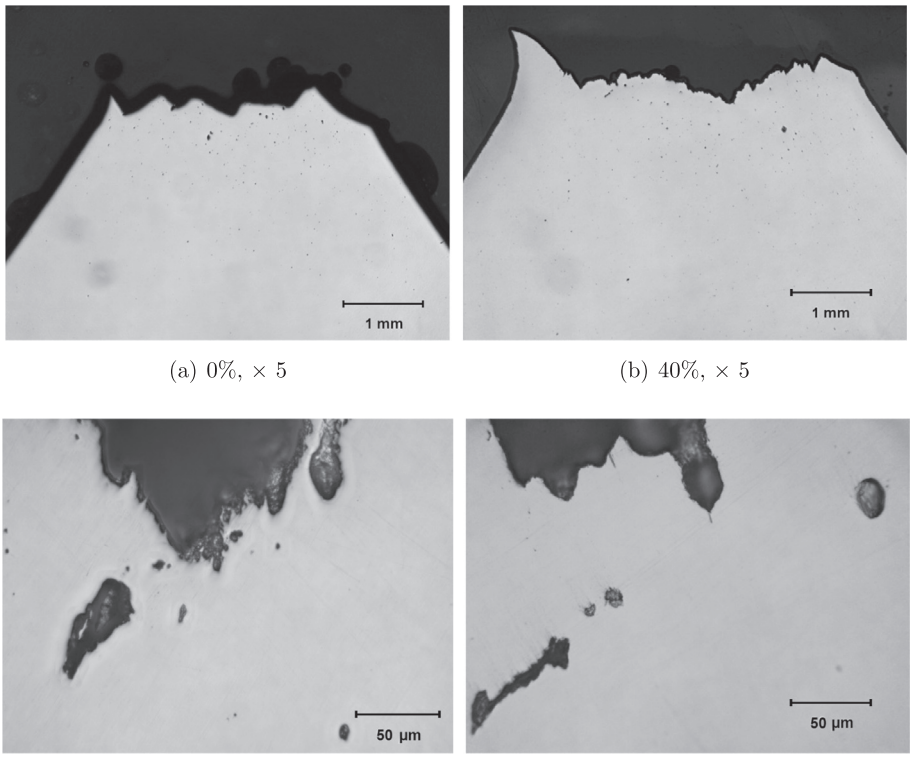

(a) 0%, × 5 (b) 40%, × 5

(c) 0%, × 50 (d) 40%, × 50

Fig. 22. Optical microscope images of cross-section at different magnification levels. Both the 0% and 40% samples are shown.

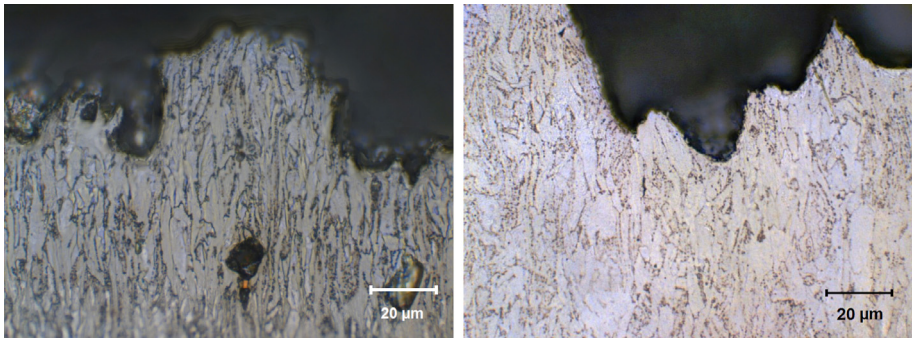

(a) Microstructure, 0% (b) Microstructure, 40%

Fig. 23. Optical microscope images of microstructure and defects in 0% specimen and 40% specimen at × 100 magnification.

40% overlapping the initial tests for comparison. In addition one specimen was attempted compressed to 100% true strain.

Again the scatter between the two parallel series was negligible. Between the two different geometries compressed to 40% and then stretched to failure, it was expected similar stress levels for corresponding strain. The fracture strain, however, should be different as the stress triaxiality σ^* is altered (Børvik et al., 2001). Stress triaxiality is defined as the ratio between the hydrostatic stress σ_H and the von Mises equivalent stress σ_{eq}, $\sigma^* = \sigma_H/\sigma_{eq}$. The stress triaxiality is dependent on both the notch radius, which in this case remained the same, and the cross-sectional diameter, which was changed from 6.4 mm to 4.0 mm – thus decreasing the triaxiality ratio (Hill, 1950). Based on the results obtained by Børvik et al. (2001), a reduction in σ^* should lead to an increase in fracture strain. This is exactly what is observed; the first geometry produced an absolute ε_f of approximately 0.5, while the latter gave about 0.8 after 40% compression.

True stress-true strain curves from the second series of tests are plotted in Fig. 24(b). Herein lies a very interesting feature: where tendencies to ductility reduction was observed in the previous tests, it is now even more evident. Compressing the specimen to 90% appears to decrease the ductility to a significant extent, also when looking at the relative deformation from load reversal to failure in tension. The mode was also altered to a 45° shear fracture, which can be seen in Fig. 25. Again the surface area at fracture tends to increase with increasing compression. Both the absolute and relative fracture strains showed the same tendencies as in Fig. 19, with the 90% specimen standing out. The SEM images revealed a ductile fracture for the 40% specimen, very similar to the surface shown in Fig. 20(b). Both the 60% and 80% specimens did show signs of cleavage fracture along the edges, examplified by Fig. 26(a) where a particle in a growing void is also shown. This indicates that ductile behaviour and large scale plasticity may precede a cleavage fracture, as noted by Smith (1968). Similar results were found for the the 90% specimen, although with less presence of cleavage fracture areas. Fig. 26(b) shows the fracture surface, with a smaller particle initiating a void. Both ductile and brittle fracture surfaces were observed, and the brittle areas showed signs of strongly elongated dimples, meaning that large plastic deformation precedes the brittle fracture.

Compressing the specimen to 100% created a slight barreling effect, causing the specimen to become widest at the centre. After stretching it to failure another 45° shear fracture was observed, although with much less indication of cleavage and an almost entirely ductile fracture. Being widest at the centre, fracture at the cross-section with lowest area or a shear fracture are more likely to occur. This lead to a questioning of the results from the 90% specimen as a similar fracture mode was observed.

4.3. Compression only

Specimens of the geometry in Fig. 18(a) were compressed to 20%, 40%, 60% and 80% plastic strain without being being stretched in tension afterwards, and then investigated in a microscope in comparison with the undeformed material. Firstly, larger voids (150–200 µm) were found in all the compressed specimens in an area outside the notched zone, i.e. in the threaded area. No voids were found in the zone where they were observed in the notched compression-tension tests (examplified by Fig. 22), which indicates that voids mainly increase in volume during tension even though they may initiate during compression close to the particles (Sabih and Nemes, 2009). The angular particles did not appear to

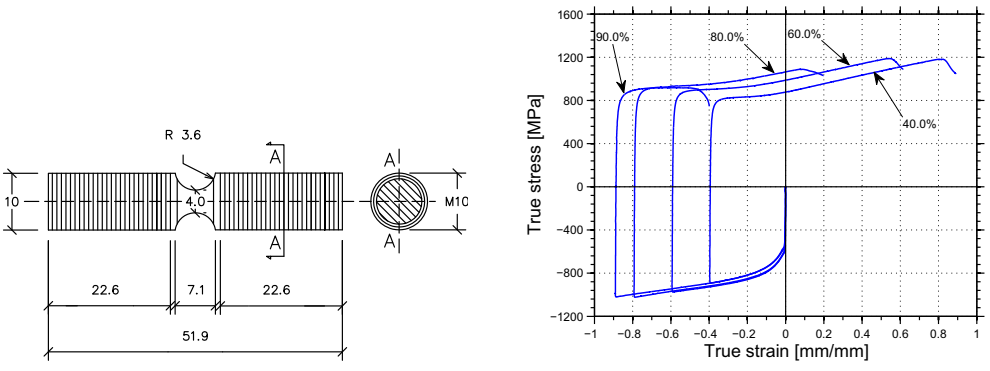

(a) Specimen geometry (b) Test results

Fig. 24. Specimen geometry (a) and results (b) from the second test series of notched compression-tension tests.

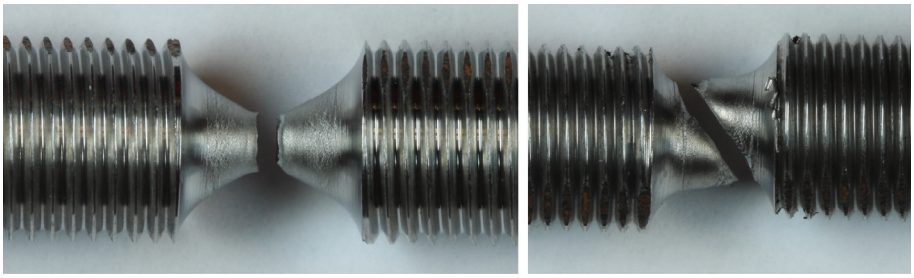

(a) 80% (b) 90%

Fig. 25. Altered fracture mode between 80% and 90% compression before tension.

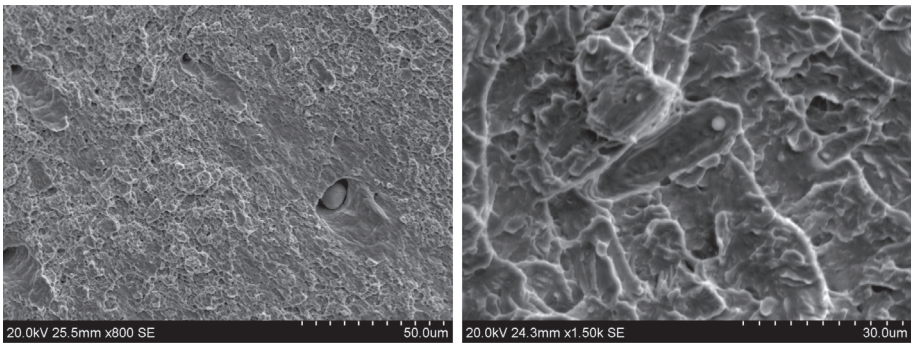

(a) 60%, × 800 (b) 90%, × 1500

Fig. 26. SEM images showing indications of both cleavage fracture and ductile behaviour in specimens compressed to (a) 60% and (b) 90%.

be affected by the deformation, while some irregularities were observed around the spherical particles. Between the different compression levels there did not seem to be any significant difference.

The 80% sample of the initial notched geometry got stuck in the test machine due to a very high force when compressed, and had to be cut out of the machine. Compression to 80% for the geometry from Fig. 24(a) was also attained, as well 90% and 100%. Observation in the microscope showed that the profile of the specimens had a slight barreling effect at 80%, and more clearly so at 90% and 100%. The microstructure had deformed quite uniformly for the 80% and 90% specimens. Images from the microscope displayed clearly visible shear bands in the microstructure of the 100% sample, confirming the assertion that the fracture mode altered due to the geometric conditions, and can thereby explain the more ductile fracture surface observed. Such localised shear bands are fracture modes that most likely will not occur in impacted pipes. Thus, the reduced ductility seen in the 90% and 100% samples seems to be an effect of the deformed specimen geometries rather than a material property, and therefore not necessarily representative for the problem at hand.

5. Discussion

Quasi-static tensile tests showed that the X65 material is both homogeneous and isotropic. Almost perfectly circular fracture surfaces from the tensile tests confirm this assertion. Component tests of the pipeline showed that the peak force during impact was fairly constant regardless of impact velocity due to the shift of deformation mode from local to global, and the mass ratio between the pipe and the trolley. Global deformation was naturally very dependent on the initial velocity since more kinetic energy has to be absorbed. So were the force–displacement curves from the subsequent stretching as well. Cracks were observed in all pipes during tension, where in the study by Manes et al. (2012) only one test displayed fracture. Very different load levels were needed to produce visible cracks, depending on the deformation from the impact. The highest impact velocities produced fracture already after impact and springback, causing cracking through 75% of the pipe's wall thickness for the highest velocity. The crack extended to the surface, but internal cracks of the same magnitude were also detected. At first the lower velocities did not seem to produce such fracture, but after a more thorough investigation in the microscope, internal cracks were indeed found without any visible signs on the surface. In this area the material appears to suffer compression to a great extent, hence the motivation for the notched compression-tension tests.

The ductile fracture observed in both the material and component tests occurs through void nucleation, growth and coalescence and is extensively discussed in the litterature over the last decades (Rice and Tracey, 1969; Thomason, 1982; Tvergaard and Needleman, 1984; Tvergaard and Hutchinson, 2002; Tian et al., 2010). Voids are often thought to initiate by particle–matrix decohesion or cracking of particles (Goods and Brown, 1979), confirmed here by the microscope images. As plastic deformation continues, voids grow in size and eventually coalesce.

Compression-tension tests on the first series of notched specimens (see Fig. 18(a)) showed a clear reduction in absolute fracture strain with increasing compression, while the relative fracture strain was less affected but still decreasing. This indicates an accelerated void nucleation (Sabih and Nemes, 2009). Microscope images showed a less deformed microstructure and more shallow dimples, also signs of earlier fracture (Ghajar et al., 2013). Cracked particles were observed, and can also contribute to this as cracks formed in particles can propagate into the surrounding ferrite (McMahon and Cohen, 1965). Voids were round and evenly shaped after compression-tension, as opposed to the rhombus shaped pores emerging from tension only. Under compression, voids

may extend perpendicularly to the load direction before growing along the load direction during tension, thus creating a more even shape (Bao and Treitler, 2004). Perpendicular void growth and/or more frequent void nucleation due to compression necessarily reduces the distance between voids, leading to earlier coalescence and provides an explanation for the more shallow pores in the specimens compressed before tension. Notwithstanding the compression, the fracture in the specimens compressed up to 40% did not transform to a brittle one as seen in the component tests where the plastic flow is more restricted. Such restricted flow conditions may increase the chances of cleavage fracture (Gao et al., 1996; Anderson, 2005).

Modifying the geometry of the notched specimens, seen in Fig. 24(a), allowed for compressive strains of 40%, 60%, 80%, 90% and even 100% to be attained. Tendencies to cleavage fracture were observed in the 60%, 80% and 90% specimens, however less so in the 100% sample. McClintock (1968) noted that cleavage planes initiated in adjacent grains rarely have a common intersection with the grain boundary, thus requiring additional deformation to cause void coalescence. This makes fracture more of a process rather than an instantaneous event. This could explain the mixture of ductile and cleavage fracture surfaces seen in these specimens, confirming that these fracture modes are not mutually exclusive (Smith, 1968). Hoagland et al. (1972) found that brittle fracture could appear highly segmented, and attributed this to isolated regions difficult to cleave. They also noted that ligaments are the main source of resistance against cleavage crack propagation.

Higher level of compression can further extend a void initiated at a cracked particle without necessarily increasing its volume, thereby requiring less tensile deformation to obtain void coalescence. Another account of the fracture could be that since the particles deform less than the matrix, stress concentrations arise around the particles. Locally the stress may be many times the yield stress, causing a ductile to brittle transition. Antretter and Fischer (1998) found through numerical investigations that if a particle is already cracked, it increases the chance of a neighbouring particle cracking due to stress concentrations, thereby initiating a cleavage fracture. A combination of decreased ligament size and increased local stress is entirely possible.

Compression only to 80% and 90% created a slight barreling effect, and an apparent uniform deformation of the microstructure. The 100% specimen exhibited barreling and clearly visible shear bands, explaining the ductile fracture surface observed. Fixing the specimens with a slightly larger diameter might ameliorate the barreling problem – an effort left for future work.

6. Conclusions

Impact and stretching tests of pipes made from an X65 offshore pipeline steel have been carried out. Straightening the pipes after impact always produced cracks. This need not be the case for lower impact velocities. SEM investigations of the fracture surface emerging first after impact revealed a brittle (cleavage) fracture, and was located on the impact side. The fracture surfaces that appeared during stretching were ductile. As fracture occurs after impact only, a pipe's axial load capacity can be greatly reduced by an impact event. Damage in the material can be difficult to assess without cutting and investigating using microscopy as it may initiate without appearing on the surface.

Compressing specimens appears to reduce ductility, and tendencies to cleavage fracture were observed on the fracture surfaces when tension was preceded by large compressive strains. Cracked particles were found as a consequence of compression. Voids may initiate during compression, leading to a more brittle fracture if allowed to grow extensively. Brittle fracture is caused by large local stresses arising from cracked particles, void nucleation on the sides of particles during compression or a combination of both. Multiple nucleation sites and extension of voids into the matrix during compression can reduce ligament size and thereby contribute to a less ductile behaviour when the load is reversed.

Acknowledgements

The present work has been carried out with financial support from the Research Council of Norway SIMLab – Centre for Research based Innovation (CRI) at the Norwegian University of Science and Technology. Thankful acknowledgement is made to Dr. Ing. Håvar Ilstad and Dr. Ing. Erik Levold at Statoil ASA for their contributions and for supplying the test material. Contributions from M.Sc. students Kjetil Slåttedalen, Anders Ørmen, Vegard Aune and Morten Hovdelien are also greatly appreciated.

References

Anderson, T., 2005. Fracture Mechanics – Fundamentals and Applications, Third ed. Taylor and Francis Group.
Antretter, T., Fischer, F., 1998. Particle cleavage and ductile crack growth in a two-phase composite on a microscale. Computational Materials Science 13, 1–7.
Bao, Y., Treitler, R., 2004. Ductile crack formation on notched Al2024-T351 bars under compression-tension loading. Materials Science and Engineering 384, 385–394.
Børvik, T., Hopperstad, O., Berstad, T., Langseth, M., 2001. A computational model of viscoplasticity and ductile damage for impact and penetration. European Journal of Mechanics A/Solids 20, 685–712.
Bouchard, P., Bourgeon, L., Lachapele, H., Maire, E., Verdu, C., Forestier, R., Loge, R., 2008. On the influence of particle distribution and reverse loading on damage mechanisms of ductile steels. Materials Science and Engineering A 496, 223–233.
Chen, K., Shen, W., 1998. Further experimental study on the failure of fully clamped steel pipes. International Journal of Impact Engineering 21, 177–202.
Cottrell, A., 1959. Fracture. Wiley, New York.
DNV, 2000. Offshore standard DNV-OSS-301: certification and verification of pipelines. Det Norske Veritas.
DNV, 2008. Offshore standard DNV-OS-F101: submarine pipeline systems. Det Norske Veritas.
DNV, 2010. Offshore standard DNV-RP-F111: interference between trawl gear and pipelines. Det Norske Veritas.
Gao, X., Shih, C., Tvergaard, V., Needleman, A., 1996. Constraint effects on the ductile-brittle transition in small scale yielding. Journal of Mechanics and Physics of Solids 44, 1255–1282.
Ghajar, R., Mirone, G., Keshavarz, A., 2013. Ductile failure of X100 pipeline steel – experiments and fractography. Materials and Design 43, 513–525.
Ghiotti, A., Fanini, S., Bruschi, S., Bariani, P., 2009. Modelling of the Mannesmann effect. CIRP Annals – Manufacturing Technology 58, 255–258.
Goods, S., Brown, L., 1979. The nucleation of cavities by plastic deformation. Acta Metallurgica 27, 1–15.
Hanssen, A., Auestad, T., Tryland, T., Langseth, M., 2003. The kicking machine: a device for impact testing of structural components. International Journal of Crashworthiness 8, 385–392.
Hanssen, A., Auestad, T., Langseth, M., Tryland, T., 2005. Development of a 3-component load cell for structural impact testing. International Journal of Mechanics and Materials in Design 2, 15–22.
Hill, R., 1950. The Mathematical Theory of Plasticity. Oxford University Press.
Hoagland, R., Rosenfield, A., Hahn, G., 1972. Mechanisms of fast fracture and arrest in steels. Metallurgical Transactions 3, 123–136.
Hyde, T., Luo, R., Becker, A., 2007. Elastic–plastic analysis of offset indentations on unpressurised pipes. International Journal of Solids and Structures 44, 399–418.
Jones, N., 2010. Inelastic response of structures due to large impact and blast loadings. Journal of Strain Analysis for Engineering Design 45, 451–464.
Jones, N., Birch, R., 1996. Influence of internal pressure on the impact behaviour of steel pipelines. International Journal of Pressure Vessel Technology 118, 464–471.
Jones, N., Birch, R., 2010. Low-velocity impact of pressurised pipelines. International Journal of Impact Engineering 37, 207–219.
Jones, N., Birch, S., Birch, R., Zhu, L., Brown, M., 1992. An experimental study on the lateral impact of fully clamped mild steel pipes. In: Proceedings of IMechE, Part E: Journal of Process Mechanical Engineering, pp. 111–127.
Kyriakides, S., Netto, T., 2000. On the dynamics of propagating buckles in pipelines. International Journal of Solids and Structures 37, 6843–6867.
Manes, A., Porcaro, R., Ilstad, H., Levold, E., Langseth, M., Brvik, T., 2012. The behaviour of an offshore steel pipeline material subjected to stretching and bending. Ships and Offshore Structures 7, 371–387.
McClintock, F., 1968. Local criteria for ductile fracture. International Journal of Fracture Mechanics 4, 101–130.

McMahon, C., Cohen, M., 1965. Initiation of fracture in polycrystalline iron. Acta Metallurgica 13, 591–604.
Ng, C., Shen, W., 2006. Effect of lateral impact loads on failure of pressurised pipelines supported by foundation. Proceedings of the Institution of Mechanical Engineers 220 (E), 193–206.
Oh, C.K., Kim, Y.J., Baek, J.H., Kim, W.S., 2007. Development of stress-modified fracture strain for ductile failure of API X65 steel. International Journal of Fracture 143, 119–133.
Palmer, A., Neilson, A., Sivadasan, S., 2006a. Pipe perforation by medium-velocity impact. International Journal of Impact Engineering 32, 1145–1157.
Palmer, A., Touhey, M., Holder, S., Anderson, M., Booth, S., 2006b. Full-scale impact tests on pipelines. International Journal of Impact Engineering 32, 1267–1283.
Ptil, Cited 23.01.2013. Damage and incidents involving load-bearing structures and pipeline systems. Petroleum Safety Authority Norway. <http://www.ptil.no/news/damage-and-incidents-involving-load-bearing-structures-and-pipeline-systems-article4306-79.html?lang=enUS>.
Rice, J., Tracey, D., 1969. On the ductile enlargement of voids in triaxial stress fields. Journal of Mechanics and Physics of Solids 17, 201–217.
Sabih, A., Nemes, J., 2009. Internal ductile failure mechanisms in steel cold heading process. Journal of Materials Processing Technology 209, 4292–4311.
Shen, W., Shu, D., 2002. A theoretical analysis on the failure of unpressurised and pressurised pipelines. Proceedings of the Institution of Mechanical Engineers 216 (E), 151–165.
Smith, E., 1968. Cleavage fracture in mild steel. International Journal of Fracture Mechanics 4, 131–145.
Statoil ASA, Cited 23.01.2013. Small gas leak from Kvitebjrn pipeline. <http://www.statoil.com/en/NewsAndMedia/News/2008/Pages/gasleakkvitebjorn.aspx>.
Tenaris, Cited 23.01.2013. Production processes. <http://www.tenaris.com/AboutUs/ProductionProcesses.aspx>.
Thomas, S., Reid, S., Johnson, W., 1976. Large deformations of thin-walled circular tubes under transverse loading – I: an experimental survey of the bending of simply supported tubes under a central load. International Journal of Mechanical Science 18, 325–333.
Thomason, P., 1982. As assessment of plastic-stability models of ductile fracture. Acta Metallurgica 30, 279–284.
Tian, R., Chan, S., Tang, S., Kopacz, A., Wang, J.S., Jou, H.J., Siad, L., Lindgren, L.E., Olson, G., Liu, W., 2010. A multiresolution continuum simulation of the ductile fracture process. Journal of Mechanics and Physics of Solids 58, 1681–1700.
Tvergaard, V., Hutchinson, J., 2002. Two mechanisms of ductile fracture: void by void growth versus multiple void interaction. International Journal of Solids and Structures 39, 3581–3597.
Tvergaard, V., Needleman, A., 1984. Analysis of the cup-cone fracture in a round tensile bar. Acta Metallurgica 32, 157–169.
Watson, A., Reid, S., Johnson, W., 1976a. Large deformations of thin-walled circular tubes under transverse loading—II: experimental study of the crushing of circular tubes by centrally applied opposed wedge-shaped indenters. International Journal of Mechanical Science 18, 387–397.
Watson, A., Reid, S., Johnson, W., 1976b. Large deformations of thin-walled circular tubes under transverse loading - III: further experiments on the bending of simply supported tubes. International Journal of Mechanical Science 18, 501–509.